Modeling and experiments of polydisperse particle clouds

Modeling and experiments of polydisperse particle clouds

Adrian C.H. Lai[1], Ruo-Qian Wang[2], Adrian Wing-Keung Law[3], and E. Eric Adams[4]

Abstract: A model for polydisperse particle clouds has been developed in this study. We extended the monodisperse particle cloud model of Lai et al. (2013) to the case of polydisperse particles. The particle cloud is first considered to be a thermal or buoyant vortex ring, with the thermal induced velocity field modeled by an expanding spherical Hill's vortex. The buoyancy of the composite thermal is assumed to be the sum of buoyancy contributed by the all particles inside the thermal. Individual particles (of different particle properties) in the cloud are then tracked by the particle tracking equation using the computed induced velocity field. The turbulent dispersion effect is also accounted for by using a random walk model. Experiments of polydisperse particle clouds were carried out to validate the model. The agreement between model predictions and experiments was reasonable. We further validate our model by comparing it with the LES study of Wang et al. (2014). The limitations of our model are then discussed with reference to the comparison. Overall, although some flow details are not captured by our model, the simplicity and generality of the model makes it useful in engineering applications.

Keywords: two-phase flows; polydisperse; buoyant vortex ring; thermals; particle clouds; integral models

1Center for Environmental Sensing and Modeling, Singapore-MIT Alliance for Research and Technology Centre, 1 CREATE Way, Singapore 138602. Email: adrian.lai@smart.mit.edu

2 Department of Civil and Environmental Engineering, University of California, Berkeley, CA 94720 , USA. Email: rqwang@berkeley.edu

3 School of Civil and Environmental Engineering, Nanyang Technological University, 50 Nanyang Avenue, 639798 Singapore. Email: cwklaw@ntu.edu.sg

4 Department of Civil and Environmental Engineering, Massachusetts Institute of Technology, Cambridge, MA 02139, USA. Email: eeadams@mit.edu

1 Introduction

There is a wide range of natural and man-made processes that involve particle-cloud dynamics. These include, for example, the dumping of dredged sediment waste into designated water zones, or dumping of sand into water for land reclamation. Pathogenic transmission resulting from coughing and sneezing has also been shown to be highly related to particle cloud dynamics (Bourouiba et al.

2014). To limit our scope, we will focus on sediment clouds that form during land reclamation and dredged material disposal (Ruggaber 2000, Zhao et al. 2012).

Sediment clouds have been the subject of a number of past investigations. It was noted by Rahimipour and Wilkinson (1992) that when a volume of particles is released into an ambient fluid of different density, it first accelerates (here termed the initial acceleration regime) and then forms a particle cloud. The particle cloud behaves as a buoyant vortex ring or 'thermal' (Turner 1957) (the thermal regime), which circulates the suspended particles about itself. It also entrains the surrounding ambient fluid, grows in radius, and decelerates. The growth rate is approximately that of a single-phase thermal when all particles are suspended inside the thermal. When the descending velocity of the thermal falls below that of the settling particles, the particles begin to settle out from the thermal. Subsequently, the particles continue to descend at the individual particle settling velocity as a bowl shaped swarm with a noticeably smaller expansion rate (Noh and Fernando 1993) - the cloud has entered the dispersive regime. After all the particles have rained out, the thermal continues to propagate as a momentum dominated vortex ring, and then subsequently grows at a much smaller expansion rate than a buoyant thermal.

Other investigations have extended the study to different release conditions that are typically encountered in the field, such as the effects of water content in the released sediments (Ruggaber 2000), and the effect of cloud momentum generated by releasing dry sediments at a height above the water surface (Zhao et al. 2012). Effects of different ambient conditions on the particle clouds were also investigated. For example, the effect of ambient stratification was studied by Noh

(2000) and Bush et al. (2003); the influence of ambient waves was studied by Zhao et al. (2013); and the crossflow effect was studied by Gensheimer et al. (2013). The two-phase characteristics of a particle cloud have been investigated by Lai et al. (2013).

These studies are useful references to develop a sediment cloud model for environmental impact assessment or operation planning of various open water sediment disposal activities. Based on the findings of these studies, Lai et al. (2013) has developed and validated a two-phase sediment cloud model by modeling the thermal as an expanding Hill's spherical vortex (Turner 1964), and tracking the particles by particle tracking equations (e.g. Eames and Gilbertson 2004). Note that most of these studies assumed that the particle clouds contain only uniform particle sizes (monodisperse releases). The more realistic case of clouds with a distribution of non-uniform particle sizes (polydisperse releases) and settling velocity has been less studied, except for some qualitative or preliminary experiments (e.g. Ruggaber 2000, Gu et al. 2008).

Several issues have to be addressed when considering polydisperse particle clouds. Preliminary experiments of Ruggaber (2000) showed that the settling of polydisperse particle clouds is markedly different than that of a monodisperse cloud. Settling patterns of polydisperse particle clouds depend on the particle size distribution. If a particle cloud consists of discrete particle sizes, several bowl shaped swarms will form due to the different settling velocity in each particle size (figure 1) – the cloud 'fractionates'. If the cloud has a continuous particle size distribution, the swarms will instead become continuous and an elongated settling particle cloud will result. Important characteristics of the cloud, such as turbidity

distribution along the water column and the deposition pattern, will be different from a truly monodisperse cloud. There have been only a few other studies that attempted to address the issues of a polydisperse particle cloud. Gu and Li (2004) performed a computational fluid dynamics (CFD) study using a two-equation turbulence closure model and particle tracking equations to predict the bulk characteristics of a particle cloud with non-uniform particle sizes. The predictions of gross characteristics were satisfactory but the phenomenon of fractionation was not seen. Wang et al. (2014) carried out a CFD study with large eddy simulation (LES) of a polydisperse cloud to obtain the detailed particle distribution during its descent. A novel higher-order numerical scheme for the two-phase simulations was proposed that enabled a larger grid spacing and thus more efficient computation. Other numerical studies include that of Harada et al. (2013), which successfully predicted the initial acceleration regime of particle releases; and Nadaoka et al. (1999), which attempted to develop a LES model coupled with a grid-averaged Lagrangian particle model for a particle plume. However, the computational resource needed was still substantial in order to yield the detailed information. Besides the high computational requirements, the lack of understanding of polydisperse particle clouds stems also from a lack of experimental data.

In this paper, we extend a monodisperse particle cloud model based on Lai et al. (2013) to predict the characteristics of a polydisperse particle cloud. A distinct advantage of the new model is the computational efficiency that makes it suitable for engineering applications. We first briefly describe Lai et al.'s (2013) model in section **2**, then its improvement and extension to a polydisperse release of particles with different size and settling velocity will be described. In section **3**,

we report the polydisperse particle cloud experiments that we carried out to validate our model. In section **4**, to further validate our model, and to better understand the strengths and limitations of our model, we compare our model predictions with Wang et al.'s (2014) LES study of a polydisperse particle cloud. The conclusion of the paper will be given in section **5**.

2 An Eulerian-Lagrangian particle cloud model

2.1 Velocity field induced by a volume of particle release

It is useful to first describe a monodisperse particle cloud release. Consider a volume of submerged monodisperse spherical sediment particle with total mass m_o and density ρ_p released from rest (with zero initial momentum) into a quiescent ambient water of density ρ_a with the acceleration due to gravity g (figure 2).

After the initial acceleration regime, the total buoyancy of the particles $B_o = m_o$ (1- $\rho_a/\rho_p)g$ induces a descending buoyant vortex ring (or thermal) structure; the fluid entrained into the buoyant vortex ring or thermal is referred to as 'fluid phase' of the sediment cloud in this study (the solid phase being the sediment particles). It has been shown both experimentally and numerically that an expanding Hill's spherical vortex (Hill 1894) can be used to approximate the mean flow field of a thermal (Turner 1964, Lai et al. 2015). When the thermal velocity w_f, radius r_f and centroid depth z_c are known (these can be predicted using an integral model, described in section **2.2**), the mean flow field in Cartesian coordinates (x,y,z) $\overrightarrow{u_f} = (u_x, u_y, u_z)$ can be expressed analytically by assuming it to be an expanding Hill's vortex. Inside the thermal [$R<r_f$, where $R^2 = x^2 + y^2 + (z - z_c)^2$], the components of the velocity are

$$u_z = -\frac{3w_f}{4}[4(\frac{x^2+y^2}{r_f{}^2}) + 2(\frac{z-z_c}{r_f})^2 - \frac{10}{3}], \quad (1)$$

$$u_x = \frac{3w_f}{2r_f{}^2}x(z-z_c), \quad u_y = \frac{3w_f}{2r_f{}^2}y(z-z_c), \quad (2)$$

and outside the thermal ($R > r_f$), the components of the velocity can be expressed as

$$u_z = \frac{w_f r_f{}^3}{2}\frac{2(z-z_c)^2 - x^2 - y^2}{[(z-z_c)^2 + x^2 + y^2]^{5/2}}, \quad (3)$$

$$u_x = \frac{3w_f r_f{}^3 x(z-z_c)}{2[(z-z_c)^2 + x^2 + y^2]^{5/2}}, \quad u_y = \frac{3w_f r_f{}^3 y(z-z_c)}{2[(z-z_c)^2 + x^2 + y^2]^{5/2}}. \quad (4)$$

The resulting flow pattern is shown in figure 2, with blue arrows representing the flow field of a Hill's vortex, and red arrows representing the flow field obtained using CFD (Lai et al. 2015). Both methods showed that a vortex ring structure is formed inside the thermal.

2.2 Integral model to predict the gross characteristics of a thermal

An integral model can be used to predict the thermal velocity w_f, radius r_f and centroid depth z_c at every time step. The thermal initially has a total buoyancy B_o with volume $V_o = m_o/\rho_p$ and total momentum $M_o = 0$. The thermal spreading rate α along depth can be expressed as $\frac{dr_f}{dz_f} = \alpha$. By noting that the volume of the thermal is $V = (4/3)\pi r_f{}^3$ and $d/dt = w_f d/dz_f$, we obtain

$$\frac{dV}{dt} = 4\pi\alpha r_f{}^2 w_f. \quad (5)$$

Although the form of the equation suggests that the entrainment into a thermal can be modeled by an inward entrainment velocity αw_f into the surface area of the thermal (similar concept of Morton et al. 1956 for a plume), it should be noted that the physical meaning of entrainment velocity is different from a plume. Here, entrainment does not mean there is an entrainment velocity directed towards the whole thermal surface; the entrainment velocity αw_f represents the outward movement of vorticity (and concentration) and not the inward movement of ambient fluid. The entrainment flow pattern is also different from a plume, with most of the entrainment taking place at the back of the thermal. The detailed entrainment flow pattern is given in the numerical study of a thermal by Lai et al. (2015). The change in total momentum M of the thermal is due to the buoyancy contributed by the particles such that

$$\frac{dM}{dt} = \frac{d}{dt}(w_f V \rho_a) = B, \qquad (6)$$

where B is the total buoyancy of the thermal. The change in vertical position is governed by the thermal vertical velocity and can be expressed as

$$\frac{dz_c}{dt} = w_f. \qquad (7)$$

We assume the buoyancy of the thermal to be the total buoyancy contributed by the particles inside the thermal. Over time, the buoyancy of the thermal decreases since the particles (as the source of buoyancy) will gradually rain out from the thermal; hence

$$B = B_o \phi, \qquad (8)$$

where ϕ is the ratio of particle number inside to that of outside the thermal. In the above equations, the thermal radius and velocity can be expressed as

$$r_f = \left(\frac{3V}{4\pi}\right)^{1/3}, \quad (9)$$

$$w_f \approx \frac{M}{\rho_a V}. \quad (10)$$

In general, a momentum dominated vortex ring only entrains fluid slowly (α ≈0.07, Lai et al. 2013), whereas a thermal entrains approximately all the fluid it passes through; the entrainment coefficient α has been shown to be a constant (≈0.25) for a single phase thermal in which buoyancy is conserved (e.g. Scorer 1958). In a particle cloud, if we defined the particle cloud number $N_c = w_s/w_f$, where w_s is the particle settling velocity, we can expect when N_c<<1, the slowly settling particles will all be suspended inside the thermal and hence the cloud will behave like a single-phase thermal; when N_c≈1 it is expected that the particles will begin to rain out, and when all particles have rained out, the vortex-ring will become momentum dominated with a much smaller growth rate. The vortex-ring will subsequently lose its momentum by the ambient drag (Maxworthy 1972). During the process of particle rain out, the buoyancy distribution will also change, which would affect the entrainment rate (from approximately 0.25 of a thermal to 0.07 of a momentum vortex ring). The relationship between α and N_c will need to be determined experimentally, and this will be reported in section 2.5.2. Eqs. (5) – (7) are then solved by the Runge-Kutta 4th order scheme to obtain the gross characteristics of the thermal.

2.3 Particle tracking equation for predicting transport of particles

With the complete flow field induced by a thermal computed by using the integral model and an expanding spherical Hill's vortex, the motion of particles can be predicted by using the particle tracking equation with the computed flow field,

which accounts for different forces acting the particle to compute the acceleration of the particle. The particle tracking equation for each particle can be expressed as (Crowe et al. 2012):

$$\rho_p V_p \frac{D\overrightarrow{u_p}}{Dt} = \overrightarrow{F_D} + \overrightarrow{F_g} + \overrightarrow{F_A} + \overrightarrow{F_I} + \overrightarrow{F_H}, \qquad (11)$$

where V_p is the volume of a particle, $\overrightarrow{u_p} = (u_p, v_p, w_p)$ is the particle velocity. The five force terms on the right hand side represent the drag, gravitational, added mass, inertial, and history forces respectively. Chan (2012) showed by a sensitivity study that the history force $\overrightarrow{F_H}$ can generally be ignored in a buoyant particle-laden flow, and so it is set to zero in the present model. The other force terms can be expressed as (Crowe et al. 2012):

$$\overrightarrow{F_D} = \frac{1}{8}\rho_a \pi d^2 C_D \left|\overrightarrow{u_f} - \overrightarrow{u_p}\right| (\overrightarrow{u_f} - \overrightarrow{u_p}), \quad (12)$$

$$\overrightarrow{F_g} = -(\rho_p - \rho_a) V_p \vec{g}, \quad (13)$$

$$\overrightarrow{F_A} = \rho_a V_p C_M \left(\frac{D\overrightarrow{u_f}}{Dt} - \frac{D\overrightarrow{u_p}}{Dt}\right), \quad (14)$$

$$\overrightarrow{F_I} = \rho_a V_p \frac{D\overrightarrow{u_f}}{Dt}. \qquad (15)$$

If we expand Eq. (11), and divide each side of the equation by the mass of the particle $\rho_p V_p$, we have

$$(1 + C_M \frac{\rho_a}{\rho_p}) \frac{d\overrightarrow{u_p}}{dt} = \frac{\mu}{8V_p} \frac{\rho_a}{\rho_p} \pi d C_D (\overrightarrow{u_f} - \overrightarrow{u_p}) \mathrm{Re}_p + (\frac{\rho_a}{\rho_p} - 1)\vec{g} + \frac{3}{2} \frac{\rho_a}{\rho_p} \frac{D\overrightarrow{u_f}}{Dt}. \qquad (16)$$

The change in particle position over time is given by

$$\frac{d\overrightarrow{x_p}}{dt} = \overrightarrow{u_p}, \qquad (17)$$

where $\overrightarrow{x_p} = (x_p, y_p, z_p)$ is the position vector of the particle; the added mass coefficient is taken as C_M =0.5 for a solid sphere; the drag coefficient is computed as $C_D = (24/\mathrm{Re}_p)(1+0.15\mathrm{Re}_p^{0.687})$ for $\mathrm{Re}_p < 1000$ and $C_D = 0.44$ for $\mathrm{Re}_p \geq 1000$ (Crowe et al. 2012), where $\mathrm{Re}_p = |\overrightarrow{u_p} - \overrightarrow{u_f}|\, d/\nu$ is the particle Reynolds number; subscripts *p* and *f* represents the 'particle' and 'fluid' properties at the location of the particle respectively; *d* is the particle diameter; and *ν* is the kinematic viscosity of water. The total acceleration $\frac{D\overline{u_f}}{Dt}$ can be obtained analytically by using a MATLAB package. An analytical expression for the total acceleration in cylindrical coordinates has been given in Lai et al. (2013). Solving Eqs. (16) – (17) gives the position of the computational particles at every time step. The integral model, with the expanding Hill's vortex (with a variable α as a function of N_c when particles are inside the vortex; and α≈0.07 when all particle rained out), and the particle tracking equations are used in sequence to obtain the characteristics of the cloud, including the frontal position z_s and the sediment cloud maximum radius r_s (figure 2).

2.4 Turbulent dispersion of particles inside the thermal

It has been observed that the particles inside the thermal are strongly mixed by the turbulence within the thermal. To account for the effects of turbulent mixing inside the thermal, we have incorporated a turbulent dispersion term in our particle tracking model using a random walk model (Kitanidis 1994):

$$\begin{aligned} x_p(t+\Delta t) &= x_p(t) + u_p \Delta t + \xi\sqrt{2D\Delta t}, \\ y_p(t+\Delta t) &= y_p(t) + v_p \Delta t + \xi\sqrt{2D\Delta t}, \\ z_p(t+\Delta t) &= z_p(t) + w_p \Delta t + \xi\sqrt{2D\Delta t}, \end{aligned} \qquad (18)$$

where ξ is a normally distributed random variable with zero mean and unit variance, and D is the dispersion coefficient, which is a constant for a particular case. In eq. (18), $\vec{u}_p \Delta t$ is the particle 'advection term' resulting from the mean flow field of the thermal, and $\xi\sqrt{2D\Delta t}$ is the 'diffusion term' as a result of the turbulence within the thermal (Wilson and Sawford 1996). To estimate D, first, the turbulent viscosity can be estimated by the mixing length model $\nu_t \sim u' l_m$, where u' is the turbulent velocity scale, and l_m is the mixing length. In the thermal regime, the velocity (and turbulence intensity) and mixing length distribution are self-similar and can be normalized by the characteristic scales w_f and r_f of the thermal, i.e $u' = \sqrt{2/3}k^{1/2} = c_1 w_f$ and $l_m = c_2 r_f$, where k is the turbulent kinetic energy and c_1 and c_2 are constants to be determined. Using the RANS simulation results of Lai et al. (2015) of a turbulent thermal (figure 3), we found that the average c_1 within the thermal is 0.35. Also, note that

$c_2 = \frac{l_m}{r_f} = \frac{\nu_t}{u' r_f} = \frac{\nu_t}{\sqrt{2/3}k^{1/2} r_f}$, and $\nu_t = C_\mu \frac{k^2}{\varepsilon}$ (where $C_\mu = 0.09$ and ε is the turbulence dissipation rate), the average value of c_2 inside the thermal can be determined to be 0.055. Further, note $w_f \approx \frac{1}{r}\sqrt{\frac{B_o}{\rho_a}}$, then we have

$\nu_t = u' l_m = c_1 c_2 \sqrt{\frac{B_o}{\rho_a}}$. Assuming a Schmidt number of 1.0 (Kuang and Lee 2006), we can estimate $D = 0.02\sqrt{\frac{B_o}{\rho_a}}$, and this is adopted in our model.

2.5 Details on the initial conditions and model implementation

2.5.1 Virtual origin and initial acceleration regime

The virtual origin is the point at which the particle cloud can be imagined to have originated if it is treated as an ideal thermal from the start (i.e. the initial acceleration regime is also modeled with the thermal behavior). It is in general not a fixed point and will vary according to different release conditions (e.g. Hunt and Kaye 2001, Zhao et al. 2012). Its variation is also due to differences in the length of the initial acceleration regime.

For our experiments of monodisperse clouds (see later section for description of the experimental setup), the plot of z_s against r_s is shown in figure 4 and the results are normalized by l_{td}, where $l_{td} = [(m_o / \rho_a) g']^{1/2} / w_s$ is the thermal-to-dispersive regime length scale ($g' = g\Delta\rho/\rho_a$ is the reduced gravity), and it is the approximate distance required for the cloud to reach the dispersive regime (Luketina and Wilkinson 1998). It can be seen that for $0.1 < l_{td} < 1$ the cloud grows almost linearly, as would be expected for a single phase thermal. By extrapolating the linear fit to $r_s = 0$, the virtual origin can be obtained as $z_{vo} \approx 0.04$ l_{td} – this is practically zero in the model implementation as our region of interest is much larger. Note that the initial acceleration regime in general needs to be considered when the region of interest is close to the source.

2.5.2 'Entrainment coefficient' of a particle cloud

The spreading rate or entrainment coefficient α of the clouds can be related to z_s and r_s by $\alpha = dr_s/dz_s$ (see section **2.2** and note that in the thermal phase $r_s \approx r_f$, $z_s \approx z_f$), where z_s is the cloud frontal depth and r_s is the corresponding maximum cloud

half-width. For monodisperse cloud with buoyancy reducing continuously due to the particle rain out, the entrainment coefficient was found to be a function of the cloud number N_c (Rahimpour and Wilkinson 1992), defined as:

$$N_c = \frac{w_s}{w_f} = w_s r_s (\frac{\rho_a}{B_o})^{1/2} . \qquad (19)$$

As discussed in section **2.2**, particles with large settling velocity typically has a large N_c closer to one, comparing to particles with small settling velocity. A plot of α against N_c for single particle type clouds is shown in figure 5 (with experimental data of this study and Lai et al. 2013). The resulting best-fit curve is

$$\alpha = 0.27(1-0.28N_c^{1.64}). \quad (20)$$

When all of the particles have rained out from the thermal (defined to be when ϕ<0.01), the spreading rate was found experimentally to be 0.07 Lai et al. (2013), which is much smaller than that of a thermal since the vortex has become momentum dominated. Hence we have

$$\alpha = \begin{cases} 0.27(1-0.28N_c^{1.64}) & \text{when } \phi \geq 0.01 \\ 0.07 & \text{otherwise} \end{cases} . \quad (21)$$

Lai et al.'s (2013) data mainly fell in the dispersive regime, and in this study more experimental data were made available in the thermal regime. Thus combining the two sets of data provides a better representation of the entrainment coefficient comparing to Lai et al. (2013) because it covers both the thermal and dispersive regimes.

2.5.3 Initial particle distribution

The particles were initially distributed uniformly in a sphere of radius $r_o = (\frac{3V_o}{4\pi})^{1/3}$ and z_c = 0. In our model we have adopted the 'discrete parcel

method' of Crowe et al. (2012), where all the particles in the parcel are assumed to have the same properties so the group is represented by one 'computational particle'. This way the number of particles used can be significantly reduced. We typically use 5000 computational particles to perform the particle tracking; the time step chosen Δt = 0.001 s; further increasing the number of particles or reducing the time step does not change the results noticeably.

2.6 Extension of model to account for polydisperse releases

The model considered in section **2.1 - 2.5** is for predicting the cloud characteristics of a monodisperse release; several modifications needed to be made for a polydisperse release (figure 6). These include:

(1) The expression of buoyancy inside the thermal

The expression for the buoyancy contributed by the particles needs to be modified since the buoyancy contribution from each type of particle may be different (each particle type in general has different density difference and volume). The generalized expression for the buoyancy remaining inside the thermal is

$$B = \sum_{i=1}^{N_{pin}} \Delta\rho_i g V_{pi}, \quad (22)$$

where N_{pin} is the number of particle inside the thermal. Here, $\Delta\rho_i$ and V_i are the density difference and volume respectively of each particle inside the thermal.

(2) The cloud number

For polydisperse particle cloud, the 'average' cloud number $\overline{N_c} = \overline{w_s} / w_f$ needs to be defined such that the polydispersity of the particles inside the thermal can be characterized. In this paper, $\overline{N_c}$ is defined by using the buoyancy weighted averaged settling velocity $\overline{w_s}$, which can be expressed as:

$$\overline{w_s} = \frac{\sum_{i=1}^{N_{Pin}} \Delta\rho_i V_{pi} g w_{si}}{\sum_{i=1}^{N_{Pin}} \Delta\rho_i V_{pi} g}, \qquad (23)$$

where w_{si} is settling velocity of individual particle. This will give the expected behaviour of a particle cloud being dominated by the 'large particles' when the mass fraction of 'fine particles' is small. The use of a buoyancy weighted average particle settling velocity can also be seen in oil and bubble plumes, where bubbles with much higher buoyancy than oil typically dominate the flow. This definition of $\overline{N_c}$ can also be shown to be the governing factor in determining whether a thermal-like or clump-like (no vortex ring formation) particle cloud will form in a polydisperse release (Er et al. 2016, under review). Ultimately, the use of $\overline{N_c}$ in our model will be justified using experimental data, as well as numerical simulations.

3 Experiments of polydisperse particle clouds

3.1 Experimental setup

Figure 7 shows the experimental setup of this study. We carried out polydisperse particle cloud experiments in a 2.4 m long x 1.2 m wide x 2.0 m deep glass tank. Different types of particles were firstly mixed in a submerged circular cylinder, open at the top, with an internal diameter of 2.0 cm. The cylinder had a bottom covered by a trap door which could be swung open when the experiments began. The measured release time of the particle cloud was only 0.4 s, which was considered to be short enough that the release could be considered instantaneous. Particles were released from rest under water in all experiments. Four distinct spherical particle types (Potters Industries BALLOTINI® Solid Glass Microspheres, metal finishing glass beads) of the same density (ρ_p = 2500 kg/m^3)

but different median diameters (and settling velocity) were used to form the composite release. Each particle type had a range of sizes in a continuous distribution and thus was not truly monodisperse. Because of the relatively large separation in size between the nominal size classes, compared to the range of sizes within a nominal size class (table 1), fractionation was expected to occur for the composite releases. The total mass of particles was 20.0 g in each experiment; different types of particles with equal mass were well mixed and submerged into water before the experiment began. A total of 9 experimental series were carried out: 1 series with a mix of 4 different particle types, 4 series with 2 particle types, and 4 series of single particle type (approximating the monodisperse case). Each experiment was repeated 10 times. The median diameter d_{50} of particles being used ranged from 0.120 mm – 0.725 mm (size A, d_{50} = 0.725 mm, size B, d_{50} = 0.514 mm, size D, d_{50} = 0.256 mm, size AE, d_{50} = 0.120 mm); the particle Reynold number $\mathrm{Re}_p = w_s(d_{50}/2)/\nu$ ranges from 1 – 77. Details of the experimental parameters, including the range of diameters for each nominal particle size, settling velocity, and particle Reynolds number can be found in table 1 – the naming follows that used by the glass bead manufacturer.

To illuminate the particle clouds, a thin and continuous laser sheet was generated by the Dantec DualPower 100-100 laser system with a laser light guide arm and a diverging cylinder. The laser sheet is aligned in a way such that it cut through the centerline plane of the cloud, and the laser light scattered by the particles was recorded using a video camera at a frequency of 30 Hz. The recorded video was converted to an image series and post-processed for analyses.

The post-processed images were analyzed and the key cloud characteristics, such as transient depth and cloud width, were obtained manually at the visual boundary of the cloud. As can be seen in figure 8, which includes typical images obtained from the experiment, the visual boundary was quite sharp, and the results were not sensitive to a reasonable change in pixel intensity threshold of the boundary. The variation resulting from individual experiments was computed based on the average results of 10 identical runs using a fixed coordinate system.

3.2 Observation

The ensemble averaged observation (10 experiments superimposed, with resulting pixel intensities averaged) of the experiment with 4 different particle types is shown in figure 8. At the beginning, the particle cloud descended as a single main body with a thermal or buoyant vortex ring structure; clouds of different particle types were not distinguishable (figure 8a). Fractionation began when the main body decelerated to approximately the settling velocity of the largest particles in the mix. In figure 8(b), particle cloud A and B rained out from the decelerating main body to form their own bowl shaped swarm, and each cloud continued to descend at approximately its own constant settling velocity (see table 1); particle cloud D and AE stayed inside the thermal, but cloud D started to show a tendency to separate by concentrating at the bottom part of the thermal. In figure 8(c), the particle cloud D finally separated from the thermal as a bowl-shaped swarm; cloud AE remained as a circulating cloud until the end of experiment. Distinct fractionation could also be observed with all other particle cloud releases with more than one particle type. For a single particle type, fractionation was not observed since the size distribution was continuous. The cloud elongation was

possibly due to the particle size distribution (and the different settling velocity of each particle size).

3.3 Comparison of model predictions and observation

3.3.1 Model visualization

An example of the model predicted polydisperse cloud motion is given in figure 9, for the same case as in figure 8 with 4 different particle types. The particle range of each type is given in Table 1. The exact size distribution of each type of particles used in the experiments is not known, and the simulations were carried out using the particle size range given in the table, assuming uniform distribution (divided into 5 bins for each particle type) by mass. Different colours represent different particle types, which helps in revealing the different particle clouds (as well as the fluid phase/thermal). Initially clouds of all particle types stayed together as a single cloud as in figure 9(a); then the cloud A with largest settling velocity rained out, followed by cloud B as in figure 9(b); and finally cloud D began to separate from the thermal (or the vortex-ring-like structure). As with the experiments, cloud AE with smallest settling velocity stayed within the thermal even close to the end of the experiments, as seen in figure 9(c). While the model is able to predict the observed 'fractionation' of particle clouds, the predicted clouds are generally descending slower than the observed clouds. For example in figure 9(c), the cloud with particle type B was observed to have reached 140 cm – 160 cm, while in our prediction it has only reached 120 cm – 140 cm, about 15% different. One reason that leads to the discrepancy is that the effects of particle interactions (such as the flow field induced by neighboring particles, and the particle group effects which essentially affect the bulk density of the particle clouds) are not accounted for in our model. Another reason is that the predictions

were made not using the exact particle size distribution. The observation suggested that the particle size could be concentrated in the higher end of the size range with higher settling velocity (indicated in table 1).

The shape of the thermal can also be compared. It can be seen from figure 8 (assuming the smallest settling particle AE is representative of the thermal shape) that the shape of the thermal is not spherical, but an oblate ellipsoid with the semi-major axis in the x- and y-direction. This was also observed in Lai et al. (2013) for a monodisperse particle cloud release. This indicates that the vortex ring generated will have some difference than a Hill's spherical vortex.

3.3.2 Key cloud characteristics

The frontal depth z_s and half-width r_s of a particle cloud are the quantities that can be determined directly from the images that we obtained experimentally, and will be used to validate our model (quantities such as cloud centroid depth will require further assumptions). Note that there were two different half-widths that we have defined. r_f is the half-width of the fluid phase, or the thermal, which was obtained by solving the thermal integral equations; and r_s is the half-width of each particle cloud (hence there will be 4 different r_s for a mix of 4 particle type releases), and was obtained as half of the furthest distance between two particles in a particle group obtained by the particle tracking equations. The repeatability of the experiments can also be assessed by comparing the average deviation of key characteristics from that of the ensemble average, which will be given in each case. Figure 10 shows the model predictions of the transient cloud depth and radius for single particle type releases. The model predictions agree reasonably well with the experimental results for the averaged frontal depth, with an average difference of about 6% for z_s. The prediction for cloud width is comparatively

poorer, with an average difference of about 16% when compared with the average. However, the predictions are still falling well within the range of experimental variation.

The comparisons between predicted and observed characteristics of bi-disperse clouds are shown in figure 11. The average difference between predictions and observations for z_s are generally within 15%. The prediction for the particle type AE in the A-AE mix (the mix with largest difference in particle size) can be seen to be particularly poor, with a difference of close to 20% (lower right of figure 11). As can be seen in the figure, the predicted slope for the cloud AE is close to that of the observation, and it is suspected that the error is due to the size A particles dragging down the cloud before separation, causing the AE particles to be 'shifted' slightly (and possibly changing the length of initial acceleration regime). This also shows that the particle cloud can behave slightly differently depending on the particle mix. The predictions of r_s has a difference of 10%-15% in general.

The prediction of a polydisperse cloud with 4 particle types is shown in figure 12. The relative difference between prediction and observation is about 10% for both z_s and r_s. Assuming a constant $\alpha = 0.25$ for the cloud in the thermal regime (0.07 in the dispersive regime) will give a difference of both the particle cloud transient depth and radius within 5% comparing to a variable α currently adopted, showing that the results are not greatly sensitive to a reasonable choice of α. In view of the various assumptions and simplifications made in the model, these predictions are considered reasonable.

In all of the figures, it can be seen that in the initial stage, when the sediment clouds were well mixed, we could not distinguish the cloud front or radius of each individual particle cloud, and so they were taken as the same as that of the mixed cloud. Fractionation of clouds was evident in all of the plots, when the data of different particle types began to separate. The model is generally able to predict the transient depth and half-width reasonably well.

4 Comparison of model predictions with LES simulations

To further validate our model, we have compared our model's predictions with the LES study of polydisperse particle clouds of Wang et al. (2014). The LES results also provided additional information of the fluid phase of a polydisperse particle cloud, which was not measured in our experiments. The LES study was carried out using the Euler-Lagrangian four-way coupling method (accounting for both particle-fluid and particle-particle interactions), using the software CFDEM, which coupled the open source CFD toolbox openFOAM with the discrete element method package LIGGGHTS (Kloss et al. 2012).

Simulation of 5 cases, each with total mass of 2.0 g , particle density 2500 kg/m^3, median particle diameter by number 0.51 mm, with different particle size range and distribution (uniform and Gaussian), were used to validate our model. The particle distribution by number is given in figure 13. A summary of the particle properties and distribution of each case is given in table 2. Exactly the same particle number and properties were used in our model predictions. The total mass

of the particles in our numerical simulations was less than that used in the present experiments, so that computational time can be substantially reduced. The particle cloud dynamics of a particle cloud with small mass can be scaled to a cloud with much larger mass using densimetric Froude scaling (Wang et al. 2015). As an example to illustrate the reduction in computational time, there will be approximately 57000 particles in 2.0 g of particles with diameter 0.3 mm, and 570000 of the same particles if the total mass is 20.0 g. For a N-particle simulation, it generally requires computational time of the order of $O[N \log(N)]$ using a tree code algorithm (e.g. Pfalzner and Gibbon 2005). Thus an estimated reduction in computational time is 12 times if 2.0 g of particles is used instead of 20.0 g.

The LES simulation results of transient frontal depth of both the solid (z_s) and fluid phase (z_f) are shown in figure 14. The depths are normalized by the length scale $L_p = \sqrt{B_o / \rho_a} / w_c$, where w_c is a characteristic velocity of the cloud. Here, w_c was defined in Wang et al. (2014) by $w_c = w_{50}$ when $t \le T_{sp}$ (thermal regime), and $w_c = w_{max}$ when $t > T_{sp}$ (dispersive regime), and $T_{sp} = 0.90 \frac{\sqrt{B_o / \rho_a}}{w_{50}^2}$ (w_{50} is the settling velocity of the median diameter particle by mass, w_{max} is the largest settling velocity in the particle mix). The model predictions, which are the average of all 5 cases, are plotted black lines in the figure 14. The solid phase transient frontal depth can be seen to be very well predicted, but that of the fluid phase is generally under-predicted by 10% - 20% in the dispersive regime, which may suggest that the increase in momentum of the fluid phase due to the particle buoyancy is greater in the LES simulation (Eq. 6). This may for example be due

to the resulting vortex not being exactly a Hill's vortex, which delayed the complete raining out of particles from the thermal.

The LES results for the transient radius growth for both the solid and fluid phase are shown in figure 15. The radius of both phases have been normalized by the length scale $L_{p2} = \sqrt{B_o / \rho_a} / w_{\max}$. Both were reasonably well predicted with the entrainment coefficient defined by eq. (21).

Finally, we have also compared the particle cloud settling patterns predicted by our model with the LES simulation. The comparisons for all 5 cases are shown in figure 16. Both our model and LES simulations predicted that the wider is the particle size range, the larger the elongation, which is an expected result due to the larger difference of particle settling velocity between the largest and smallest particle (of the same density). However, the extent of the elongation predicted by the model is slightly greater than that of the LES simulation. Similar observation on cloud elongation can also be made if we compare the model predictions with experiments (figure 8 and 9). The interaction between particles, such as the vertical velocity induced by surrounding particles, and the bulk density resulted as a descending particle group, were not accounted for in our model. This would partly explain the discrepancy between our model and experiments or LES cloud settling pattern (in the dispersive regime).

It can also be seen that the model generally predicts a cloud front shape that is more 'bowl-like' than the flat shaped simulated by LES. This is due to the fact that the actual vortex ring generated by particles simulated by LES is not exactly like a Hill's vortex, but another vortex causing less 'roll-up' of particles before raining out from the thermal.

In terms of computational time, our model required 500 s to complete a simulation using a single core; LES required 5 hours for the same case using 32 cores each with comparable CPU speed as we used in our model. At the sacrifice of some of the flow details, our model is typically of the order of 1000 times faster than LES with similar computer configuration. This is particular attractive for engineering applications where an efficient and reasonably accurate predictions are required.

5 Conclusions

A model for polydisperse particle clouds has been developed by extending the modeling framework of Lai et al. (2013) for monodisperse particle clouds. The particle mix is initially modeled as a thermal or buoyant vortex ring, with the velocity field computed by approximating the thermal or buoyant vortex ring as an expanding Hill's spherical vortex. The rate of growth of the thermal radius in the thermal phase is assumed to be a function of cloud number, and was obtained experimentally. The growth rate of the vortex ring in the subsequent dispersive regime was obtained experimentally by Lai et al. (2013), and was found to be much smaller than that in the thermal regime. The particle tracking equation is then used to track the motion of particles with the different forces acting on different particle types. The variation of buoyancy with time is also accounted for by summing the contribution of buoyancy of all particles inside the thermal.

Experiments were carried out to validate the model. Particle mixes with 2 – 4 distinct particle types were released underwater, and key characteristics such as transient depth and radius of each individual particle cloud were measured. In all cases, 'fractionation' (clouds with different particle sizes raining out) happened in an order from big particles to small ones. The model can capture this phenomenon

and reproduce the key characteristics within the range of experimental uncertainty. The experiments were carried out using a fixed mass (and buoyancy) of particles (20.0g) and only four types of particles were tested. The results, however, can be extended to releases of other mass or buoyancy by considering dynamic similarity scaling (Wang et al. 2015).

We further validated our model by comparing the model predictions with the LES study of polydisperse particle clouds by Wang et al. (2014). The predicted key cloud characteristics are generally in reasonable agreement with the LES results, except for some differences in the details of the flows. For example, our model does not account for the interaction between particles, and the particles induced vortex would not be a perfect Hill's vortex. These caused some results predicted by our model, for example the cloud settling pattern, to be different from the LES predictions. Nonetheless, noting that our model is on the order of 1000 times faster than LES in completing a simulation, our model will still be useful in many engineering applications, where efficient and reasonably accurate predictions are often needed.

While the formation of a particle cloud as a thermal, close to the release source, has been considered in details by many investigators, the far-field fate and transport of the particle cloud is also important, e.g., for evaluating the environmental impact due to the turbidity caused by fine particles released to coastal waters. Such evaluations require the coupling between near-field and far-field hydrodynamic models. The model presented here provides a simple, yet powerful tool for the analysis of the near-field particle cloud dynamics, which can link to a far-field model. An extension of the model to account for the effect of

ambient stratification is also possible with the proposed cloud buoyancy variation formula. The coupling of near and far field sediment cloud models, and the effect of ambient stratification, will be the focus of our future studies.

Acknowledgements

This research was supported by the National Research Foundation Singapore through the Singapore MIT Alliance for Research and Technology's Center for Environmental Sensing and Modeling interdisciplinary research program.

Compliance with Ethical Standards

We declare that our work submitted is compliance with the ethical standards as required by the journal.

Conflict of Interest: The authors declare that they have no conflict of interest.

Research involving Human Participants and/or Animals: The authors declare that this study involved no human participants and/or animals.

Informed consent: The authors declare that consent to submit has been received explicitly from all co-authors.

Adrian C.H. Lai

Research Scientist
Centre for environmental sensing and modelling
Singapore-MIT Alliance for Research and Technology Centre

References

1. Bourouiba L, Dehandschoewercker E, Bush JWM (2014) Violent expiratory events: on coughing and sneezing. J Fluid Mech 745:537-563

2. Bush JWM, Thurber BA, Blanchette F (2003) Particle clouds in homogeneous and stratified environments. J Fluid Mech 489:29-54

3. Chan SN (2012) Mixing and deposition of sediment-laden buoyant jets. PhD Thesis, Department of Civil Engineering, The University of Hong Kong.

4. Crowe CT, Schwarzkopf JD, Sommerfeld M, Tsuji Y (2012) Multiphase Flows and Droplets and Particles. CRC Press.

6. Eames I, Gilbertson MA (2004) The settling and dispersion of small dense particles by spherical vortices. J Fluid Mech 498:183-203

7. Er JW, Zhao B, Law AWK and Adams EE. (2016) Formation of composite sediment clouds. J Fluid Mech, under review.

8. Gensheimer, R.J., Adams, E.E. and Law, A.W.K. (2013) Dynamics of particle clouds in ambient currents with application to open water sediment disposal. J. Hydraulic Engineering, ASCE 139(2): 114-123

9. Gu J, Li CW (2004) Modeling instantaneous discharge of unsorted particle cloud in ambient water by an Eulerian-Lagrangian method. J Hydr Res: 42(4):399-405

10. Gu J, Huang J, and Li CW (2008) Experimental study on instantaneous discharge of unsorted particle cloud in cross-flow. Journal of hydrodynamics, 20(1):10–16

11. Harada E, Tsuruta N, Gotoh H (2013) Two-phase flow LES of the sedimentation process of a particle cloud. J Hydr Res: 51(2):186-194

12. Hill MJM (1894) On a spherical vortex. Philos Trans Roy Soc London Ser A 185:213-245

13. Hunt GR, Kaye NG (2001) Virtual origin correction for lazy turbulent plumes. J Fluid Mech 435:377-396

14. Kitanidis PK (1994) Particle-tracking equations for the solution of the advection-dispersion equation with variable coefficients. Water Resources Research, 30(11), 3225–3227

15. Kloss C, Goniva C, Hager A, Amberger S and Pirker S (2012). Models, algorithms and validation for opensource DEM and CFD-DEM. Prog. Comput. Fluid Dynam. Int. J. 12(2): 140 – 152.

16. Kuang CP and Lee JHW (2006). Stability and Mixing of a Vertical Axisymmetric Buoyant Jet in Shallow Water. Environmental Fluid Mechanics, 6(2): 153 – 180.

17. Lai ACH, Zhao B, Law AWK and Adams EE (2013). Two-phase modeling of sediment clouds. Environmental Fluid Mechanics, 13(5): 435 – 463.

18. Lai ACH, Zhao B, Law AWK and Adams EE (2015). A numerical and analytical study of the effect of aspect ratio on the behavior of a round thermal. Environmental Fluid Mechanics, 15(1): 85 – 108.

19. Luketina D, Wilkinson D (1998) The transition to the swarm phase for a particle cloud. Proc. 13th Australasian Fluid Mechanics Conference, Melbourne, Australia.

20 Maxworthy T (1972) The structure and stability of vortex rings. J Fluid Mech 51: 15 – 32

21. Morton BR, Taylor G, Turner JS (1956) Turbulent Gravitational Convection from Maintained and Instantaneous Sources. Proc. R. Soc. Lond. A 234(1196): 1-23

22. Nadaoka K, Nihei Y, Yagi H (1999). Grid-averaged Lagrangian LES model for multiphase turbulent flow, Int. J. Multiphase Flow, 25(8): 1619-1643

23. Noh Y (2000). Sedimentation of a particle cloud across a density interface. Fluid Dyn Res 27: 129 – 142

24. Noh Y, Fernando HJS (1993) The transition in the sedimentation pattern of a particle cloud. Phys Fluids A 5:3049 - 3055

25. Pfalzner S and Gibbon P (2005) Many-Body Tree Methods in Physics, Cambridge University Press.

26. Rahimipour H, Wilkinson D (1992) Dynamic behaviour of particle clouds. Proc. 11th Australasian Fluid Mechanics Conference, Hobart, Australia.

27. Ruggaber GJ (2000) The dynamics of particle clouds related to open-water sediment disposal. PhD Thesis, Department of Civil and Environmental Engineering, Massachusetts Institute of Technology

28. Turner JS (1957) Buoyant vortex ring. Proc R Soc Lond A 239: 61-75

29. Turner JS (1964) The flow into an expanding spherical vortex. J Fluid Mech 18(2):195-208

30. Wang RQ, Law AWK and Adams EE (2014). LES study of settling particle cloud dynamics, Int. J. Multiphase Flow, 67: 65-75

31. Wang RQ, Adams EE , Law AWK, Lai ACH, (2015) Scaling Particle Cloud Dynamics: From Lab to Field. J. Hydraulic Engineering, ASCE 141(7): 06015006

32. Wilson JD and Sawford BL, (1996) Review of Lagrangian stochastic models for trajectories in the turbulent atmosphere. Bound.-Layer Meteor 78: 191 - 210

33. Zhao B, Law AWK, Adams EE, Shao D, Huang Z (2012) Effect of air release height on the formation of sediment thermals in water. J. Hydraulic Research 50(5): 532-540

33. Zhao B, Law AWK, Huang Z, Adams EE, Lai ACH (2013) Behavior of Sediment Clouds in Waves. J. Waterw. Port Coast. Ocean Eng. 139(1):24-33

Figure 1: Model simulation of a polydisperse particle cloud. Fractionation can be observed in this simulation.

Figure 2: A monodisperse particle cloud and the flow field it induced (blue arrows: Hill's vortex; red arrows: CFD simulation of a thermal).

Figure 3: The CFD simulation results of a thermal (Lai et al. 2015): (a) Contours of the normalized turbulence intensity $c_1 = \frac{\sqrt{2/3}k^{1/2}}{w_f}$; (b) Contours of the normalized eddy viscosity $c_2 = \frac{\nu_t}{\sqrt{2/3}k^{1/2}r}$.

Figure 4: Experimentally observed normalized cloud frontal depth versus the normalized cloud half-width.

Figure 5: Experimentally observed particle cloud spreading rate versus cloud number; solid line is the best-fit of data.

Figure 6: A polydisperse particle cloud in quiescent ambient.

Figure 7: Experimental setup of this study

Figure 8: Typical observation in polydisperse particle cloud experiments (ensemble averaged images): (a) Time t = 3.0 s; (b) t = 10.1 s; (c) t = 14.3 s. Letters represent particles of different diameter and settling velocity (Table 1)

Figure 9: Model predictions of the polydisperse particle cloud experiments: (a) time t = 3.0 s; (b) t = 10.1 s; (c) t = 14.3 s. Blue: size A, Red: size B, Green: size D, Black: size AE, black circle: fluid phase.

Figure 10: Transient depth and half-width of monodisperse particle clouds. Lines: prediction; symbols: observation. Solid line is z_s; dashed line is r_s.

Figure 11: Transient depth and half-width of bi-disperse particle clouds. Lines: prediction; symbols: observation. Colors represent different particle size, and are same as Figure 9. Solid line is z_s; dashed line is r_s.

Figure 12: Transient depth and half-width of a polydisperse particle cloud (mix of 4 sizes). Lines: prediction; symbols: observation. Colors represent different particle size, and are same as Figure 8. Solid line is z_s; dashed line is r_s.

Figure 13: Particle distribution of all the 5 cases of Wang et al. (2014)'s LES study.

Figure 14: Comparison of model predicted and LES simulated transient frontal depth of both the (a) solid; and (b) fluid phase. Symbols: LES results; black line: average of model predictions.

Figure 15: Comparison of model predicted and LES simulated transient cloud radius of both the (a) solid; and (b) fluid phase. Symbols: LES results; black line: average of model predictions.

Figure 16. Comparison of (a) model predicted and (b) LES simulated particle cloud settling patterns of polydisperse releases (snapshot at time = 6 s). From left to right: Case Bu1, Bu2, Bu3, Bg1, Bg2.

Type (Potters designation)	**m_o (g)**	**d (mm)**	**Particle density** (kg/m^3)	**Settling velocity of d_{50} (cm/s)**	**Particle Reynolds number**	**Color in the figures**
A	20.0	0.60 – 0.85	2500	10.6	76.6	Blue
B	20.0	0.425 – 0.60	2500	7.2	36.8	Red
D	20.0	0.212 – 0.30	2500	2.9	7.5	Green
AE	20.0	0.09 – 0.150	2500	0.9	1.1	Black
A + AE	20.0	mixed	2500	mixed	-	-
B + D	20.0	mixed	2500	mixed	-	-
D + AE	20.0	mixed	2500	mixed	-	-
A + B	20.0	mixed	2500	mixed	-	-
A + B + D + AE	20.0	mixed	2500	mixed	-	-

Table 1: Experimental parameters in this study. More information of the Potters designation of the glass beads can be found at Potters Industries' website: http://www.pottersbeads.com/LinkClick.aspx?fileticket=wuI3dYsWav8%3d&tabid=291&mid=1009 (Retrieved April 2016).

Case	Distribution by particle number	d (mm)	d_{50} (mm)	Particle density (kg/m^3)	w_{50} (cm/s)	w_{max} (cm/s)
Bu1	Uniform	0.26 – 0.73	0.61	2500	8.8	10.6
Bu2	Uniform	0.26 – 0.76	0.64	2500	9.3	11.2
Bu3	Uniform	0.43 – 0.60	0.53	2500	7.6	8.7
Bg1	Gaussian	0.45 – 0.57	0.52	2500	7.4	8.3

Bg2	Gaussian	0.22 – 0.81	0.57	2500	8.2	12.0

Table 2: Summary of the properties of particles used in the numerical simulation of Wang et al. (2014)

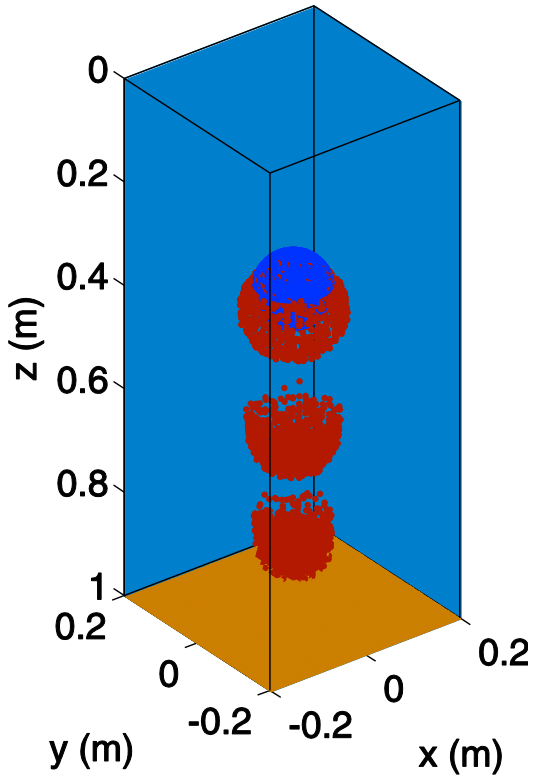

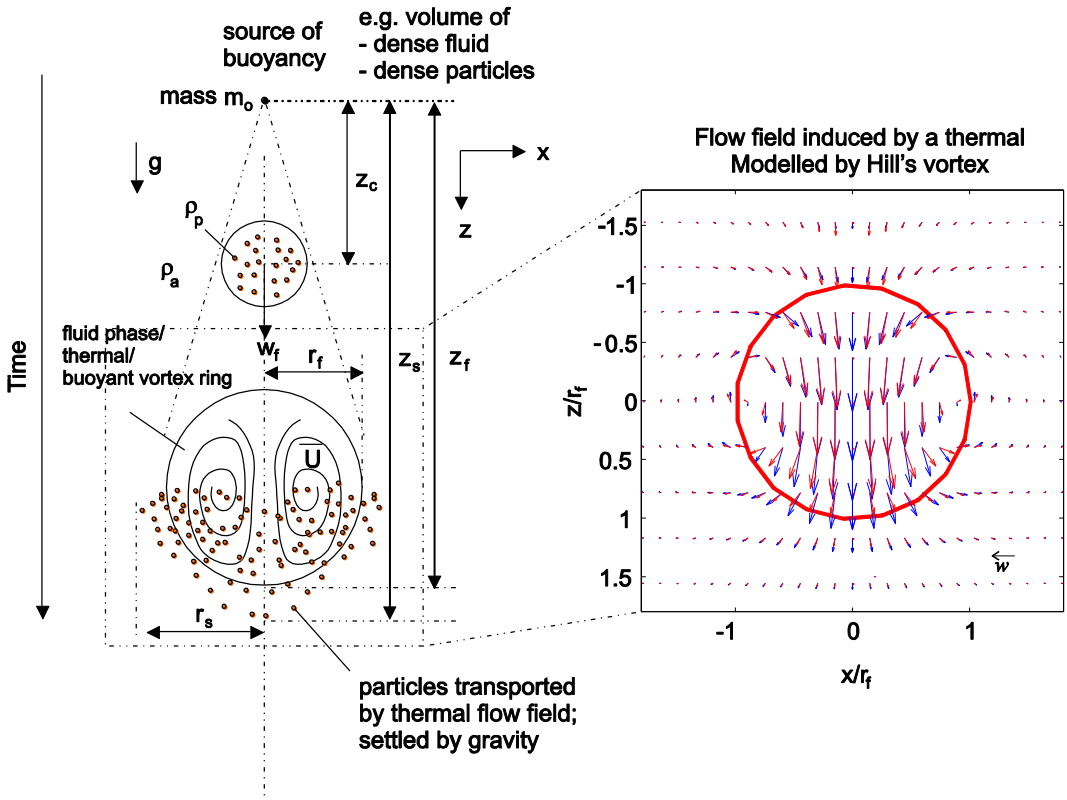
source of buoyancy
e.g. volume of
- dense fluid
- dense particles
mass m_o
g
ρ_p
ρ_a
z_c
x
z
Time
fluid phase/
thermal/
buoyant vortex ring
w_f
r_f
z_s
z_f
$\bar{U}$
r_s
particles transported
by thermal flow field;
settled by gravity
Flow field induced by a thermal
Modelled by Hill's vortex
z/r_f
x/r_f
w

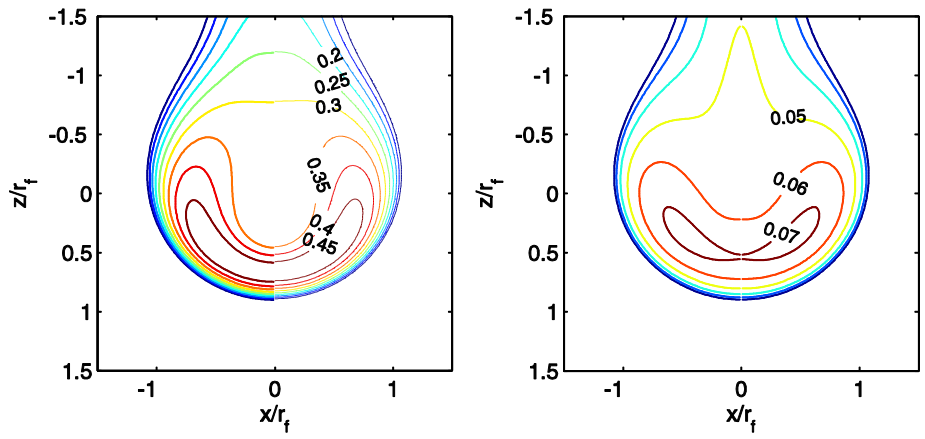
z/r_f
x/r_f
0.2
0.25
0.3
0.35
0.4
0.45
0.05
0.06
0.07

(a) (b)

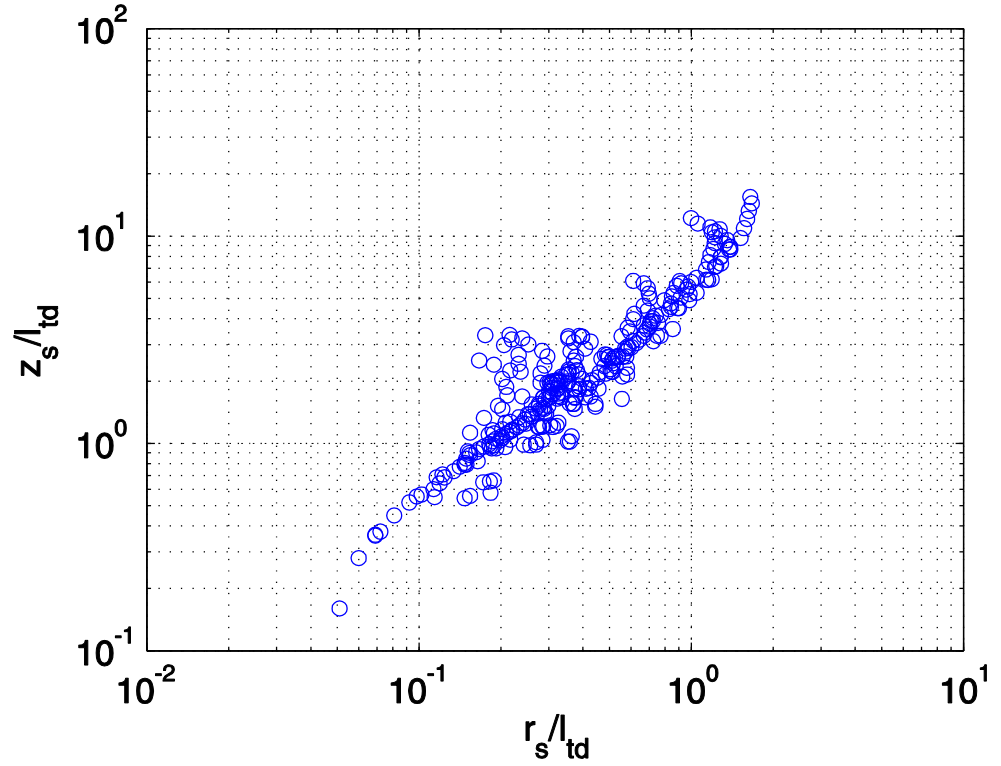
10^2
10^1
10^0
10^{-1}
z_s/l_{td}
10^{-2}
10^{-1}
10^0
10^1
r_s/l_{td}

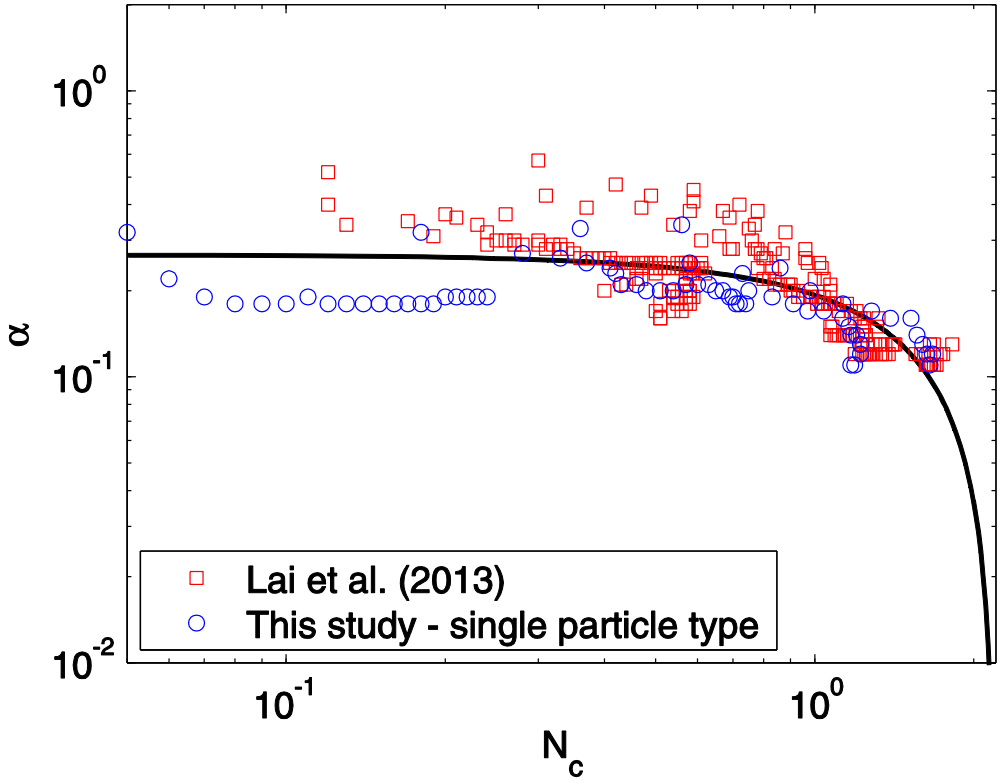
10^0
10^{-1}
10^{-2}
α
Lai et al. (2013)
This study - single particle type
10^{-1}
10^0
N_c

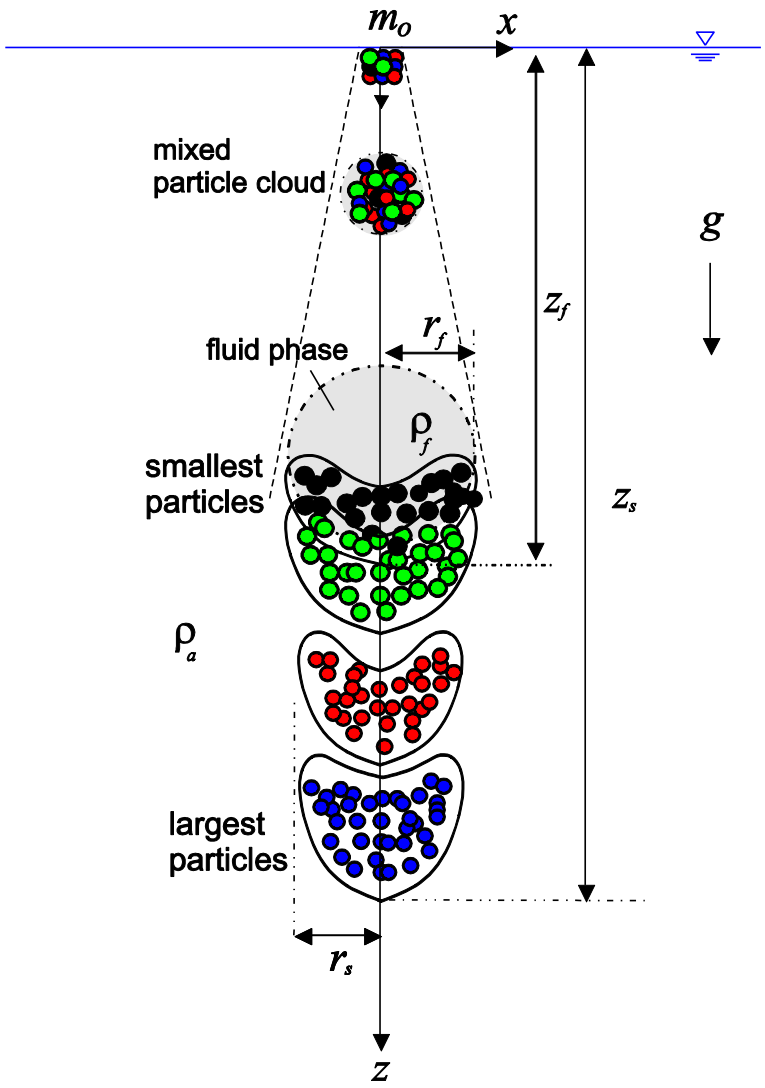
m_o
x
mixed
particle cloud
g
z_f
r_f
fluid phase
ρ_f
smallest
particles
z_s
ρ_a
largest
particles
r_s
z

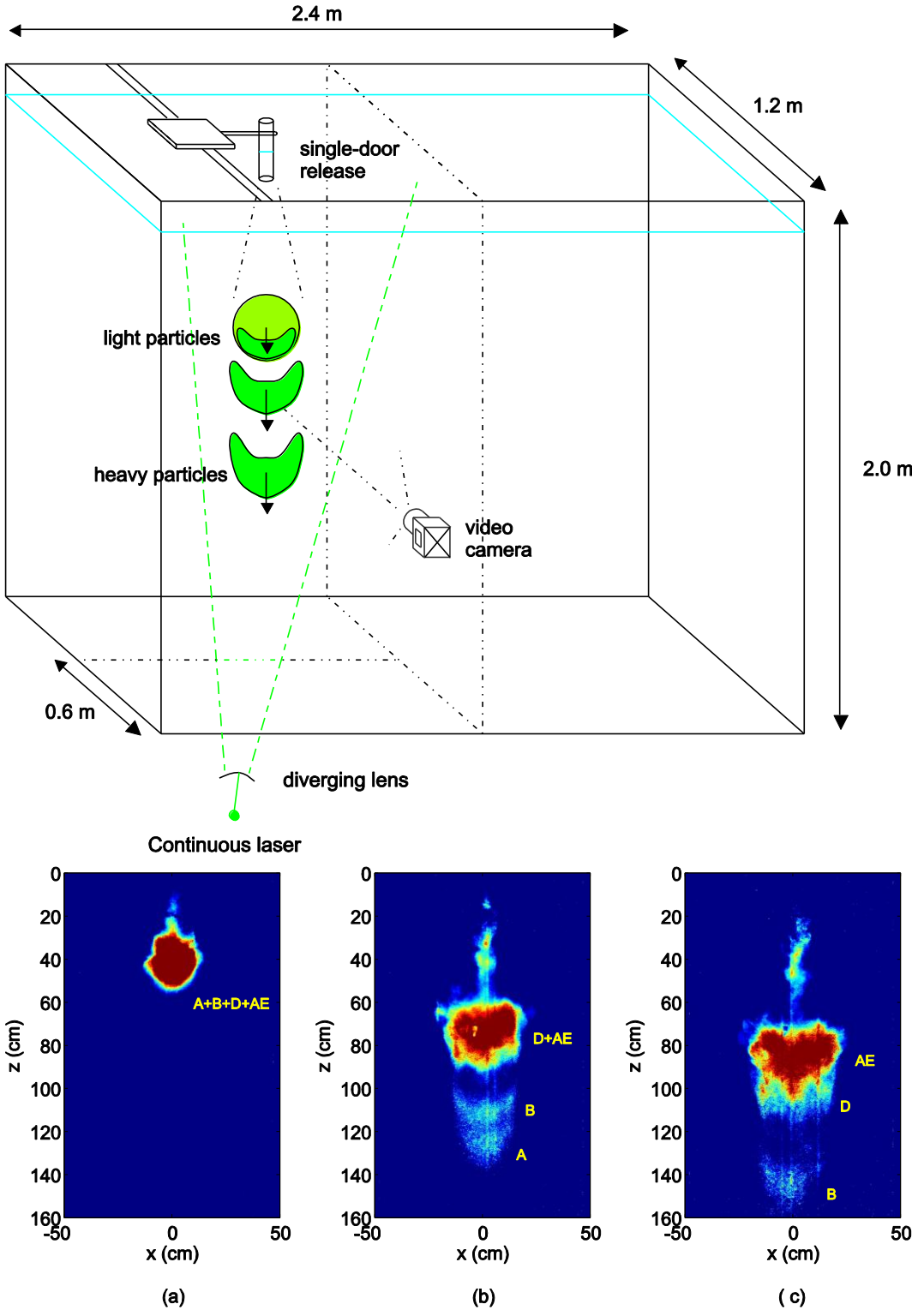
2.4 m
1.2 m
single-door
release
light particles
heavy particles
video
camera
2.0 m
0.6 m
diverging lens
Continuous laser
z (cm)
x (cm)
A+B+D+AE
D+AE
B
A
AE
D
B
(a)
(b)
(c)

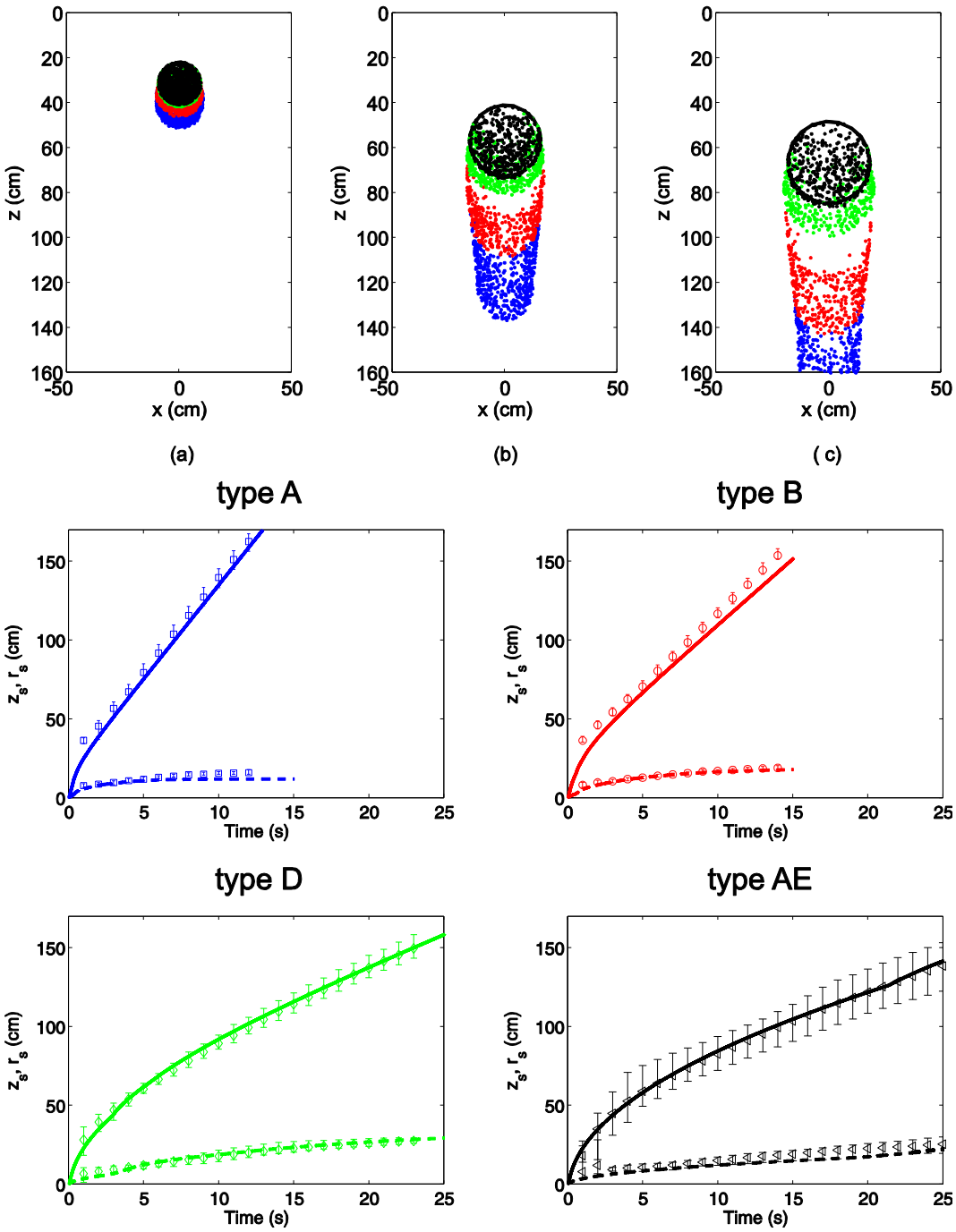
z (cm)
x (cm)
(a)
(b)
(c)
type A
type B
type D
type AE
z_s, r_s (cm)
Time (s)

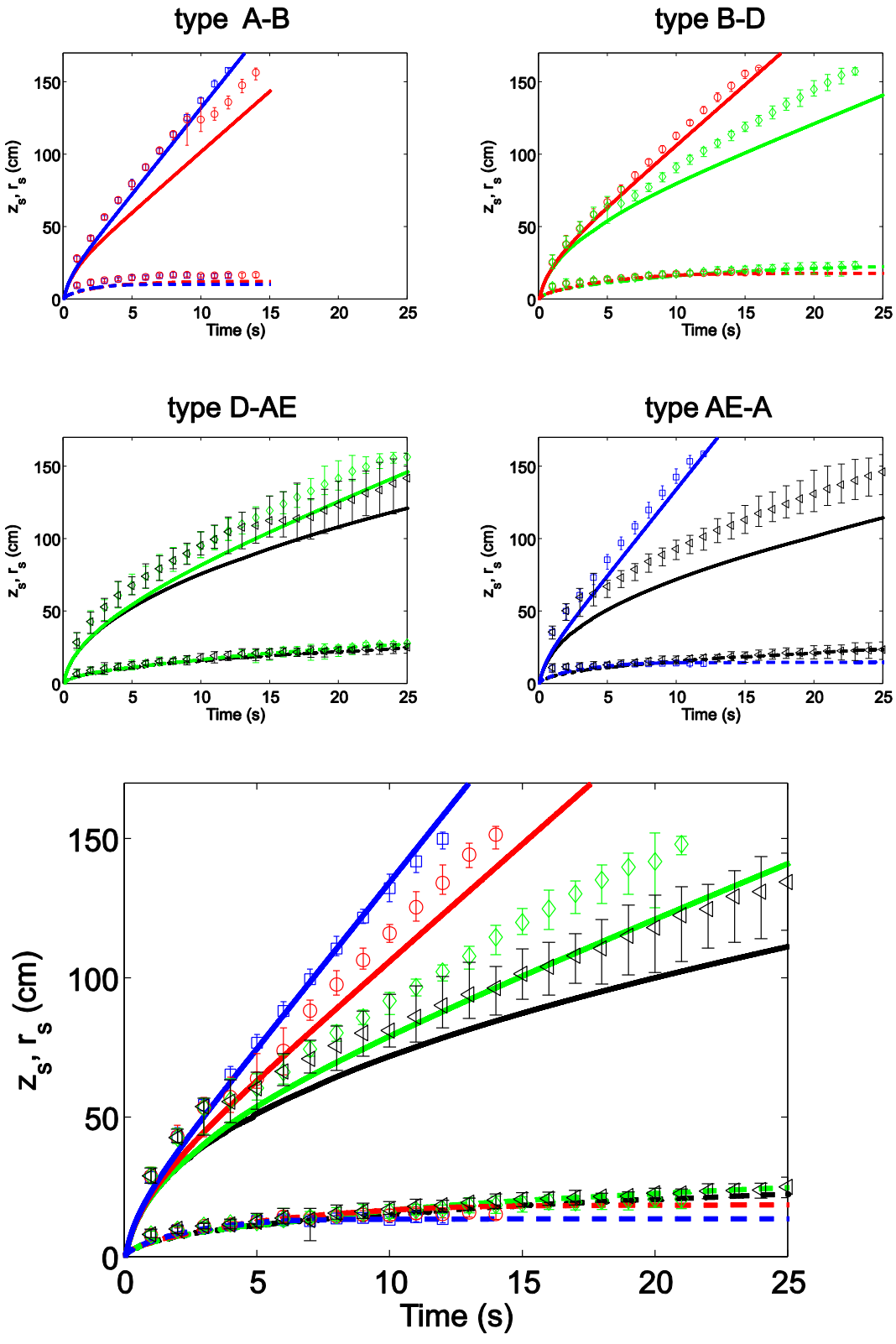
type A-B
type B-D
type D-AE
type AE-A
z_s, r_s (cm)
Time (s)
0
50
100
150
0
5
10
15
20
25

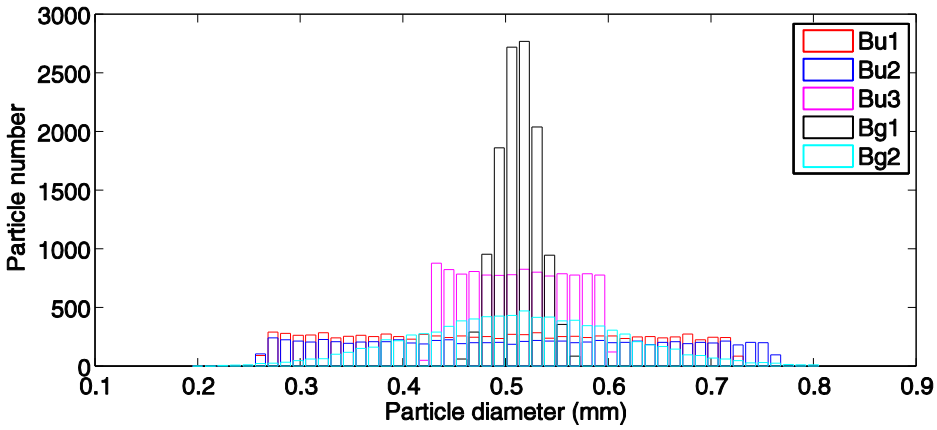
Particle number
Particle diameter (mm)
Bu1
Bu2
Bu3
Bg1
Bg2

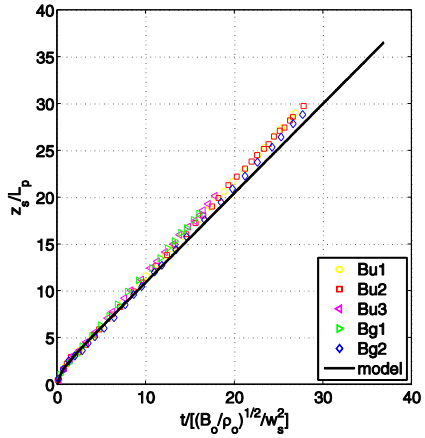
z_s/L_p
$t/[(B_o/\rho_o)^{1/2}/w_s^2]$
Bu1
Bu2
Bu3
Bg1
Bg2
model

(a)

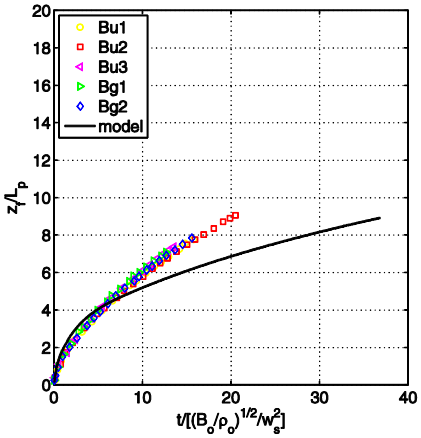
z/L_p
$t/[(B_o/\rho_o)^{1/2}/w_s^2]$
Bu1
Bu2
Bu3
Bg1
Bg2
model

(b)

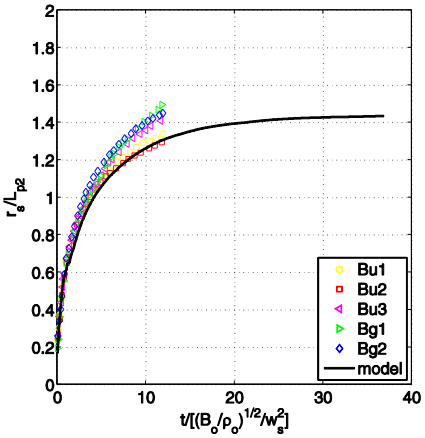
r_s/L_{p2}
$t/[(B_o/\rho_o)^{1/2}/w_s^2]$
Bu1
Bu2
Bu3
Bg1
Bg2
model

(a)

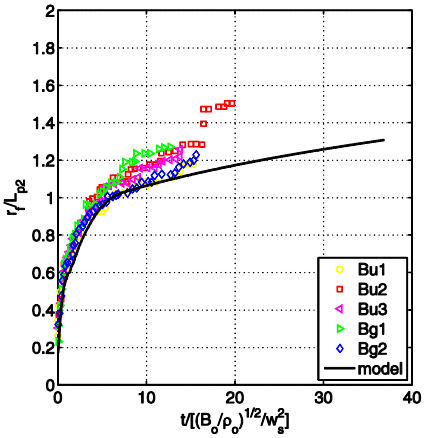
r/L_{p2}
$t/[(B_o/\rho_o)^{1/2}/w_s^2]$
Bu1
Bu2
Bu3
Bg1
Bg2
model

(b)

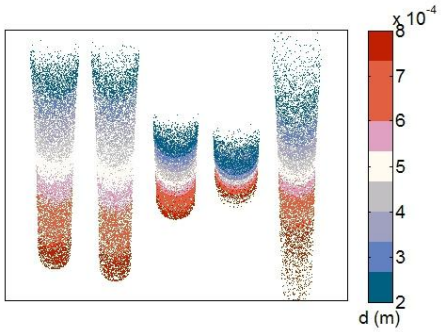

(a)

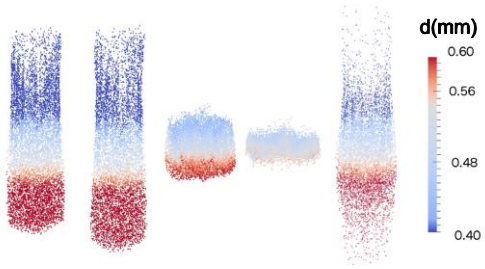

(b)